Journal of Materials Chemistry A

ROYAL SOCIETY OF CHEMISTRY

PAPER

View Article Online
View Journal | View Issue

Check for updates

Cite this: J. Mater. Chem. A, 2025, 13, 4429

Synergistic dual-defect band engineering for highly efficient photocatalytic degradation of microplastics *via* Nb-induced oxygen vacancies in SnO_2 quantum dots†

Jianqiao Liu, [ad] Dan Zhao,[b] Xian Wu,[a] Di Wu,[a] Ningning Su,[a] Yang Wang,[a] Fang Chen,[c] Ce Fu, *[a] Junsheng Wang *[a] and Qianru Zhang*[d]

Received 24th October 2024
Accepted 31st December 2024

DOI: 10.1039/d4ta07579j

rsc.li/materials-a

The band structure is a crucial consideration in designing semiconductor photocatalysts, particularly as their size has been continuously decreasing over the past few decades. However, the bandgap of nanostructures is usually broadened due to quantum confinement effects, fundamentally inhibiting their photocatalytic performance. Herein, we demonstrate synergistic dual-defect band engineering in SnO_2 quantum dots. Nb is incorporated to induce the creation of oxygen vacancies in the SnO_2 crystal lattice. The synergistic mechanism between dual defects is elucidated through their interactive formation and collective contribution of the band structure. Nb impurities establish donor levels within the bandgap, while the gap between donor levels and the conduction band is filled by the induced oxygen vacancies, effectively extending the conduction band edge to the Fermi level. This design of dual-defect engineering not only narrows the bandgap but also provides abundant defect states for electron transitions and increases the lifetimes of photogenerated carriers, thereby facilitating highly efficient visible-light-driven photocatalytic degradation of microplastics, even in realistic aqueous environments. Furthermore, the intermediate products and photodegradation pathways of microplastics are comprehensively elucidated. The synergistic dual-defect band engineering not only achieves highly efficient visible-light-driven photocatalytic degradation of microplastics, but also introduces a comprehensive design framework for tuning band structures in nanoscale photocatalysts.

1. Introduction

Microplastics (MPs) impose significant risks to ecosystems due to their diverse sources,[1,2] widespread presence,[3,4] potential ecological impacts[5,6] and persistence in various ecosystems,[7–10] necessitating urgent measures for their elimination. The UN Environmental Assembly has begun organizing negotiations on the first legally binding international instrument to end plastic pollution, which is expected to be completed by the end of 2024.[11] Photocatalysis represents a promising technique for the removal of MPs from aquatic environments[12] as it is able to degrade a wide range of MPs[13] with environmental friendliness,[14,15] flexibility in implementation[16] and more importantly, capability for *in situ* operation[17,18] under sole solar energy harvesting, simultaneously achieving pollution reduction and carbon emission reduction. In pursuit of such sustainable remediation strategies, selecting a photocatalyst with inherent chemical stability, scalable defect tunability, and robust photochemical performance is of paramount importance.

The band structure of semiconductor photocatalysts is crucial for their application in the photodegradation of MPs, as it has direct influences on degradation efficiency.[19–21] In this context, SnO_2 quantum dots (QDs) have attracted considerable attention due to their intrinsic chemical inertness, non-toxicity, and robust structural stability, along with their favorable electronic configuration and high surface area, all of which are beneficial for photocatalytic applications.[22] Compared to other common semiconductor photocatalysts, SnO_2 offers a broader conduction band edge and superior chemical resilience, facilitating the generation of reactive oxygen species that can effectively break down MPs into environmentally benign intermediates. Furthermore, the inherent oxygen vacancies (V_O) in SnO_2 provide a significant opportunity to control the

[a]College of Information Science and Technology, Dalian Maritime University, Dalian 116026, Liaoning, China PR. E-mail: fuce_dlmu@sina.com; wangjsh@dlmu.edu.cn; Fax: +86 411 84729934; Tel: +86 411 84729934

[b]School of Transportation, Department of Roadway Engineering, Southeast University, Nanjing, 211189, Jiangsu, China PR

[c]Center of Advanced Optoelectronic Materials, College of Materials and Environmental Engineering, Hangzhou Dianzi University, Hangzhou, 310018, China

[d]Institute of Agriculture Resources and Regional Planning, Chinese Academy of Agricultural Sciences, Beijing 100081, China PR. E-mail: zhangqianru@caas.cn

† Electronic supplementary information (ESI) available. See DOI: https://doi.org/10.1039/d4ta07579j

structure–property correlations.[23,24] In recent years, the reduction in size of these photocatalysts, particularly with the advent of QDs, has markedly enhanced their performance.[25,26] However, many QD photocatalysts, including SnO_2 QDs, possess excessively large band gaps, resulting in low visible light utilization, thus limiting their practical applications.[27,28] To address this issue, defect engineering and band structure engineering have emerged as promising strategies to enhance the visible light absorption and overall photocatalytic efficiency of these nanoscale semiconductors.[29–32]

Quantum confinement effects are the fundamental cause of bandgap broadening in nanostructures, thereby inhibiting their photocatalytic performance.[33,34] Recent advancements have been achieved by tailoring the structure and composition of QDs, including precise size control, introduction of oxygen defects, and doping with foreign elements, to optimize the band structure.[35–39] Specifically, SnO_2 QDs have been extensively studied, and various modification strategies such as metal doping and oxygen vacancy creation have led to significant improvements in their photocatalytic activity.[40,41] These approaches fine-tune the band structure and introduce strategically positioned defect states, thereby not only improving charge-carrier dynamics but also enhancing the formation of reactive species essential for effective MP degradation. Notably, the construction of impurity levels through defect engineering has emerged as a promising method for band structure modification.[42–44] Nevertheless, the low density of defect states in confined QDs restricts the carrier transition efficiency, thereby limiting the separation efficiency of photogenerated electron–hole pairs and significantly affecting overall photocatalytic efficiency.[45] The incorporation of dual defects,[46–48] which can introduce abundant defect states within the bandgap, presents a potential strategy to substantially enhance the performance of QD photocatalysts.

The innovative design of this work focuses on the implementation of synergistic dual-defect band engineering in SnO_2 QDs to enhance their photocatalytic performance. Previous research has demonstrated that V_O and metal doping can effectively optimize the performance of QD photocatalysts.[49–51] Among metal dopants, Nb has been identified as a promising candidate due to its ability to create donor levels and facilitate oxygen vacancy formation in SnO_2 QDs.[52] By leveraging Nb-induced defect states, the inherently favorable band structure of SnO_2 is harnessed to further enhance charge-carrier utilization and reactive species generation, thereby maximizing the degradation efficiency toward MPs. Synergistic dual-defect incorporation integrates these approaches by simultaneously introducing V_O and metal dopants, thereby creating more complex and beneficial defect states. This strategy has led to significant improvements in light absorption, carrier separation efficiency, and overall photocatalytic activity in recent investigations.[53–55] Nevertheless, the interaction mechanisms between dual defects are not well understood, specifically regarding their formation mechanisms and synergistic effects. Moreover, the detailed mechanisms of dual-defect band engineering, including the formation and positioning of defect states and their influence on the whole band structure, remain inadequately explored. To address these challenges, this work proposes a synergistic defect design by introducing V_O through Nb doping and aims to systematically elucidate the interaction mechanisms of dual defects and the underlying principles of band engineering. Through this approach, we aim to further enhance the photocatalytic performance of SnO_2 QDs and provide novel theoretical insights into dual-defect band engineering.

Herein, this study introduces the incorporation of Nb doping and V_O creation in SnO_2 QDs to achieve synergistic dual-defect band engineering, with the aim of enhancing their photocatalytic performance under visible light. Nb-doped SnO_2 QDs are synthesized, and their structural, compositional, and electronic properties are systematically investigated. *In situ* characterization techniques are employed to analyze the behaviors of photogenerated electrons and holes as well as their impacts on photocatalytic efficiency, providing a detailed examination of the formation and distribution of defect states and their influences on the entire band structure. The photocatalytic capability of the QDs in degrading MPs under visible light is comprehensively assessed, including the intermediate products and photodegradation pathways, which substantiates the effectiveness of the dual-defect band engineering approach. This work not only underscores the intrinsic adaptability and stability of SnO_2 as a photocatalytic platform but also offers a robust theoretical and practical framework for dual-defect engineering, ultimately advancing the rational design of high-performance catalysts for sustainable MP remediation.

2. Materials and methods

2.1. Preparation of undoped and Nb-doped SnO_2 QDs

The photocatalysts of undoped and Nb-doped SnO_2 QDs were prepared by a hydrothermal process as previously described,[56,57] as shown in Fig. 1(a). Stannous chloride dihydrate ($SnCl_2 \cdot 2H_2O$) and thiourea (CH_4N_2S) were dissolved and mixed in deionized water at a molar ratio of 10 : 1. The solution was stirred in a magnetic stirring apparatus at 25 °C for 24 hours. During this time, SnO_2 QDs were obtained through the hydrolysis–oxidation process, which was accelerated by the tautomerism between thiourea and isothiourea.[58] Additionally, a specific amount of ammonium niobate oxalate hydrate ($C_4H_4NNbO_9.nH_2O$) was incorporated into the solution at Nb/Sn molar ratios of 0%, 3%, 6%, 9% and 12%. The Nb-doped solution was then transferred to a Teflon autoclave and subjected to the hydrothermal process at 180 °C for 6 hours, allowing the incorporation of Nb ions into the crystal matrix of SnO_2 QDs. Consequently, *n*Nb-SnO_2 QD solutions (n = 0%, 3%, 6%, 9%, and 12%) were obtained.

2.2. Photocatalytic degradation of MPs

The polyethylene (PE) fragments with an average size of 350 μm were used as typical MPs. 50 mg of PE was mixed with 40 mL of deionized water in a quartz vessel. Then, a 4 mL solution of 6% Nb–SnO_2 QDs containing 0.2 mol L^{-1} Sn atoms was added. After a 30-minute dark treatment, the vessel was exposed to visible light from an 8 W LED (400–800 nm) and a 200 W Xe lamp (380–

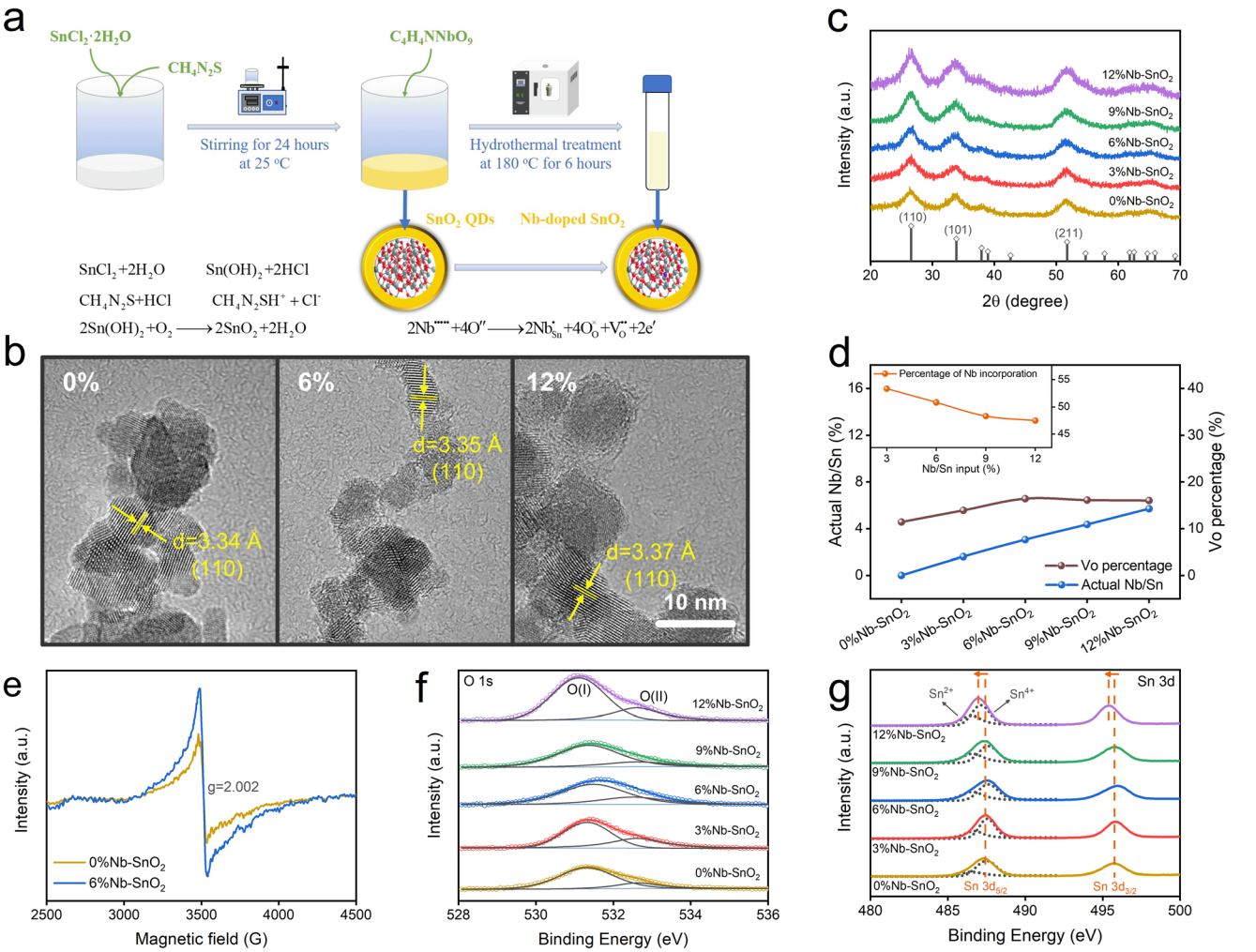

Fig. 1 Synthesis and microstructural properties of SnO_2 QDs with Nb-induced V_O: (a) schematic illustration of the preparation procedure; (b) HRTEM morphologies; (c) XRD patterns; (d) stoichiometry of SnO_2 QDs with dual defects; (e) ESR spectra; (f) XPS O 1s spectra; (g) XPS Sn 3d spectra.

1100 nm), respectively. The resulting mixture was filtered, leaving behind the PE fragments, which were dried at 50 °C for 3 hours. The remaining PE fragments were weighed to determine the photocatalytic degradation efficiency, calculated using eqn (1).

$$\text{PE efficiency}(\%) = \frac{M_0 - M}{M_0} \times 100\% \quad (1)$$

Here, M_0 and M indicated the mass of PE before and after photocatalytic degradation, respectively.

The surface morphology of PE was observed using an optical microscope (NMM-800RF, Zhejiang Saide Instruments, China) and a field emission scanning electron microscope (FESEM, Sigma 500, ZEISS, Germany). The infrared absorption was measured using a Fourier transform infrared spectrometer (FTIR, Bruker Tensor27, Bruker Scientific Technology, Germany). The total organic carbon (TOC) analysis was carried out using a carbon/nitrogen analyzer (Vario TOC Cube, Elementar, Langenselbold, Germany). The gaseous final product of MP degradation was collected and analyzed using gas chromatography (GC, GC7920, Beijing China Education Aulight Technology Co. Ltd, China).

The potential applicability of visible-light driven photocatalytic degradation of PE in real-world scenarios was evaluated by using various water matrices, such as recycled water, lake water and seawater. Recycled water was supplied by Dalian Water Group Co., Ltd in accordance with mandatory standards of GB 5749–2022, which imposed limitations of Na^+ < 200 mg L^{-1}, Fe^{3+} < 0.3 mg L^{-1}, Al^{3+} < 0.2 mg L^{-1}, chloride < 250 mg L^{-1} as well as sulfate < 250 mg L^{-1}. The lake water was collected at Xinhai Lake originating from Lingshui River in Dalian, China. It contained total nitrogen (0.7 mg L^{-1}), total phosphorus (0.03 mg L^{-1}), sulfides (0.15 mg L^{-1}) and metal ions of Cu^{2+} and Zn^{2+} at concentrations below 1.0 mg L^{-1}. The seawater was collected from Lingshui Bay in Yellow Sea, Dalian, China. The primary solutes included cations of Na^+ (11.04 mg L^{-1}), K^+ (0.4 mg L^{-1}), Ca^{2+} (0.42 mg L^{-1}) and Mg^{2+} (1.33 mg L^{-1}) as well as anions of Cl^- (19.86 mg L^{-1}) and SO_4^{2-} (2.77 mg L^{-1}). Filters were employed to remove possible organisms and impurities from

lake water and seawater before investigating photocatalytic activities.

2.3. *In situ* characterization under irradiation

Photocurrent measurements were carried out on an electrochemical workstation with a three-electrode system (CHI660E, Shanghai Chenhua Instrument Co., Ltd, China) comprising a working electrode of indium tin oxide (ITO), reference electrode of Ag/AgCl and counter electrode of a Pt mesh. The light source was a 300 W Xe lamp. The *in situ* XPS characterization was conducted using an AXIS Supra+ (Shimadzu, Japan) system equipped with a 300 W light source, CME-TLSX300UV-2G (Microenergy Beijing Technology Co., Ltd China), which supported continuous tunable wavelengths ranging from 200 to 1100 nm. The measurement was first carried out in the dark. Then, after switching on the light source, the subsequent tests were completed at the wavelengths of 550 nm, 420 nm and 260 nm, respectively.

2.4. Determination of active radicals and intermediates

Trapping experiments were conducted with radical scavengers to identify the primary active radicals involved in the photocatalytic process. Four analytical reagents, namely isopropyl alcohol (IPA), potassium bromate ($KBrO_3$), ammonium oxalate monohydrate ($(NH_4)_2C_2O_4$) and *p*-benzoquinone (BQ), were employed as scavengers to eliminate active radicals of hydroxyl species ($^{\bullet}OH$), electrons (e^-), holes (h^+) and superoxide species ($O_2^{\bullet-}$). Each scavenger was added at a concentration of 0.02 mol L^{-1} to a 4 mL solution at the start of the photocatalytic degradation process. Furthermore, electron spin resonance (ESR) spectra were also used to determine the active radicals of $^{\bullet}OH$ and $O_2^{\bullet-}$ in the photocatalytic degradation of PE. Gas chromatography-mass spectrometry (GC-MS, Agilent 7890, Agilent, USA) was used to identify the intermediate products of PE degradation during photocatalytic degradation.

2.5. DFT computational methodology

The electronic properties of the band structure and energy levels in SnO_2 before and after Nb incorporation were investigated using density functional theory (DFT). All calculations were performed using the Device Studio platform with the DS-PAW package. The Perdew–Burke–Ernzerhof (PBE) functional, which described the exchange–correlation interaction within the generalized-gradient approximation (GGA), was employed for these calculations.[59,60] The calculations were performed in reciprocal space to enhance speed and accuracy. The computational model was constructed based on the tetragonal unit cell of rutile SnO_2 with lattice constants of $a = b = 4.7373$ Å and $c = 3.1864$ Å. A $2 \times 3 \times 3$ supercell, containing 36 Sn atoms and 72 O atoms, was created and cleaved along the (110) facet due to its lowest surface energy.[61]

The supercell was modified to match the stoichiometry and electrical properties of the experimental undoped and Nb-doped SnO_2 QDs, ensuring similarity with actual samples. In the undoped SnO_2 simulation, 7 O atoms were removed from the supercell to create V_O. On the other hand, in the Nb-doped SnO_2 supercell, 12 O atoms were eliminated and 2 Sn atoms were substituted with Nb. Schematic illustrations of the supercells are presented in Fig. S1.† A 15 Å thick vacuum layer was added to prevent interactions between adjacent layers. Prior to geometry optimization, the *k*-point Monkhorst–Pack mesh was set to $2 \times 1 \times 1$, and the energy cut-off was set to 400 eV. The convergence energy threshold for self-consistent iteration was set to 10^{-6} eV. Additionally, the internal stress was constrained to be below 0.05 GPa. During the geometric optimization, the maximum force and displacement were set to 0.03 eV $Å^{-1}$ and 0.001 Å, respectively. The valence electrons considered for the respective elements in the calculation were as follows: Sn $5s^25p^2$, O $2s^22p^4$ as well as Nb $4s^14p^34d^5$. To address the underestimated band gap issue,[62] the Hubbard parameter (U) was incorporated using the GGA + U method,[63] enabling accurate reproduction of electronic properties. The total density of states (TDOS) and partial density of states (PDOS) were extracted for all elements. The valence band edge (E_V) and conduction band edge (E_C) were determined by using the occupied and unoccupied TDOS, respectively.

The adsorption energy of metal cations on the (110) surface of the Nb-doped oxygen-deficient supercell was calculated based on the adsorption model shown in Fig. S2.† Various possible metal cations in actual water matrices were considered, such as Na^+, K^+, Ca^{2+}, Mg^{2+}, Zn^{2+}, Cu^{2+}, Fe^{3+} and Al^{3+}. The adsorption energy for an individual metal cation (E_{ads}) was calculated using eqn (2).

$$E_{ads} = E_{cation/surface} - (E_{cation} + E_{surface}) \quad (2)$$

Here, $E_{cation/surface}$ denoted the total energy of the supercell with the adsorbed cation. E_{cation} and $E_{surface}$ were the energy of the cation and semiconductor surface, respectively. The negative value of E_{ads} indicated that the adsorption was exothermic and was likely to be spontaneous.

3. Results and discussion

3.1. Defect engineering of Nb-induced V_O creation in SnO_2 QDs

The defect engineering of Nb-induced V_O creation in SnO_2 QDs is conducted through a controlled two-step process, as shown in Fig. 1(a). Initially, the hydrolysis of $SnCl_2$ is accelerated by thiourea and $Sn(OH)_2$ undergoes an oxidation reaction, converting to SnO_2 QDs. During the subsequent hydrothermal treatment, $C_4H_4NNbO_9 \cdot nH_2O$ is introduced, facilitating the substitutional incorporation of Nb ions into the SnO_2 lattice. The doping mechanism is considered to be a charge-compensated process, wherein Nb ions replace Sn ions due to their similar ionic radii of 0.64 Å and 0.69 Å, respectively. The substitution creates oxygen defects and free electrons to maintain charge neutrality, as described by the defect reaction equation in eqn (3).[64] The incorporation of Nb into the SnO_2 lattice facilitates V_O creation, which is anticipated to enhance the electronic and optical properties, making them suitable for a variety of applications.

$$2Nb^{\cdot\cdot\cdot\cdot\cdot} + 4O'' \rightarrow 2Nb^{\cdot}_{Sn} + 4O^{\times}_{O} + V^{\cdot\cdot}_{O} + 2e' \quad (3)$$

Here, $Nb^{\cdot\cdot\cdot\cdot\cdot}$ and $Nb^{\cdot}_{Sn}$ represent the ionized Nb site and the Nb atom substituting Sn sites. O'', $O_O\times$ and V_O indicate the ionized oxygen site, the lattice oxygen and the oxygen vacancy, respectively.

The influences of Nb incorporation on the lattice structure of SnO_2 QDs are further discussed through morphological and microstructural aspects. The HRTEM morphologies are presented in Fig. 1(b), where the average grain size increases from 3.9 to 6.1 nm with Nb dopant concentration. The distinct lattice fringes of the (110) facet are observed and the spacing exhibits a slight expansion from 3.34 Å to 3.37 Å because of the Nb incorporation, indicating lattice distortion of the SnO_2 matrix. The crystalline structures are identified through XRD patterns in Fig. 1(c). The characteristic peaks at 2θ positions of 26.5°, 33.8°, 37.9°, and 51.7° are ascribed to the (110), (101), (200), and (211) planes, indicating the rutile structure of the SnO_2 matrix (JCPDS 01-077-0448). No individual phases of niobium oxides are observed, suggesting that Nb primarily exists in its ionic form. The peaks for progressive Nb doping suggest changes in lattice parameters due to the difference in ionic radii between Nb^{5+} and Sn^{4+} ions. The substitutional incorporation of Nb^{5+} ions into the SnO_2 lattice likely induces lattice strain and alters the crystallite size, which is quantitatively analyzed using the Scherrer formula.[65] These results are consistent with the grain sizes observed from the HRTEM morphologies in Fig. 1(b).

Nb incorporation has a significant impact on the stoichiometry of Nb-doped SnO_2 QDs. In general, the XPS survey spectra in Fig. S3(a)† confirm the presence of Sn, O, and Nb and the EDS spectra in Fig. S4† also confirm the increasing amount of Nb at 2.166 keV, along with O, Sn, S, and Cl elements, of which the latter two are the residuals of $SnCl_2$ and CH_4N_2S precursors. Due to their trace concentration and water-soluble nature, the residual S and Cl species exert negligible influence on the photocatalytic performance in an aqueous environment. Moreover, ICP-OES indicates that the actual Nb/Sn ratios are 53.3–47.5% of the designed Nb amount in the precursors, as shown in Fig. 1(d) and Table S1.† This suggests that during the hydrothermal treatment, approximately half of the Nb is incorporated into the SnO_2 matrix as the crystallites grow. The Nb 3d peaks at 207.25 eV and 210.2 eV, shown in Fig. S3(b),† exhibit increased intensities with higher Nb doping levels, indicating the presence of Nb ions in the SnO_2 matrix. The Nb/Sn atomic ratio can be evaluated by integrating the peak areas of each element, coinciding with the ICP-OES results. The spatial uniformity of Nb dopants both on the surface and in the bulk of SnO_2 QDs is inferred. This conclusion is also supported by the elemental mapping from HAADF-STEM in Fig. S5.†

The existence of V_O is confirmed by the ESR spectra in Fig. 1(e), where a significant enhancement of the V_O signal is observed at $g = 2.002$ for 6%Nb–SnO_2 QDs compared to the undoped sample. The density of V_O is evaluated by using the O 1s spectra in Fig. 1(f), which are deconvoluted using the Gaussian–Lorentzian function to identify sub-peaks centered at 531.38 eV and 532.58 eV. The former, labeled as the O(I) type, corresponds to O atoms with full coordination with Sn atoms (tetravalent SnO_2). The latter, denoted as the O(II) type, is attributed to nonstoichiometric coordination between Sn and O atoms (divalent SnO), which are commonly employed as an indirect indicator of V_O. The density of V_O is estimated based on the integrated areas of these sub-peaks, as summarized in Table S1.† As Nb doping increases, it initially elevates the V_O concentration from 11.4% of undoped SnO_2, to 6%Nb–SnO_2 exhibiting a maximal V_O density of 16.4%. This substantial V_O density is likely to enhance the semiconductive properties by facilitating charge carrier generation and transport. However, the V_O density does not continue to increase beyond 6% Nb incorporation, presumably due to the lattice distortion induced at higher doping levels, which constrains further V_O formation. Furthermore, the shift of O 1s peaks in Fig. 1(f) suggests the formation of Nb–O bonds.

Fig. 1(g) shows double peaks at 495.92 eV and 487.52 eV, corresponding to Sn $3d_{3/2}$ and Sn $3d_{5/2}$, respectively. Extensive Nb doping of over 12% causes a slight red shift of the peaks to 495.71 eV and 487.31 eV, indicating that the defects lead to distortion of the SnO_2 crystal lattice.[66] Therefore, it is concluded that Nb incorporation leads to lattice distortion associated with the slightly smaller ionic radius of Nb compared to Sn.[67] The ionic Nb dopants facilitate the creation of V_O by the mechanism of charge compensation. Upon deconvolution of the Sn $3d_{5/2}$ spectrum, distinct Sn^{2+} and Sn^{4+} sub-peaks are identified, thereby confirming the presence of nonstoichiometric O coordination in the Nb-doped SnO_2 QDs. This observation corroborates the O 1s spectra in Fig. 1(f), which accurately reflects the existence of oxygen vacancies through the associated nonstoichiometric coordination of divalent oxide.

3.2. Synergistic dual-defect band engineering and optical–electrical properties

The synergistic effects of dual defects on the band structure of SnO_2 QDs are comprehensively investigated. Fig. 2(a) illustrates the Tauc plot relationship used for bandgap evaluation from the UV-vis absorbance of each Nb-doped SnO_2 QD, as presented in Fig. S6.† The bandgap of Nb-doped SnO_2 QDs exhibits a negative dependence on the amount of Nb added, ranging from 4.76 eV for undoped SnO_2 to 2.18 eV for 12% Nb–SnO_2. The incorporation of Nb has minimal influence on the position of E_V, as depicted in the XPS valence spectra shown in Fig. 2(b). Fig. 2(c) displays the band structure of each Nb-doped SnO_2 QD. The dependence of the band structure on Nb incorporation indicates that Nb atoms primarily affect the conduction band, resulting in lowered energy level positions with increasing Nb.

The band structure engineering by dual defects has a significant impact on the optical–electrical properties. The photoluminescence (PL) of Nb-doped SnO_2 QDs at an excitation wavelength of 280 nm is shown in Fig. 2(d). Emission peaks are observed at 311 nm, and the peak intensity varies with incorporation of Nb, exhibiting a reverse volcano-shaped correlation. 6% Nb–SnO_2 exhibits the weakest PL emission, suggesting the highest possibility of photo-electrical transition and the lowest recombination of photogenerated carriers. The PL decay

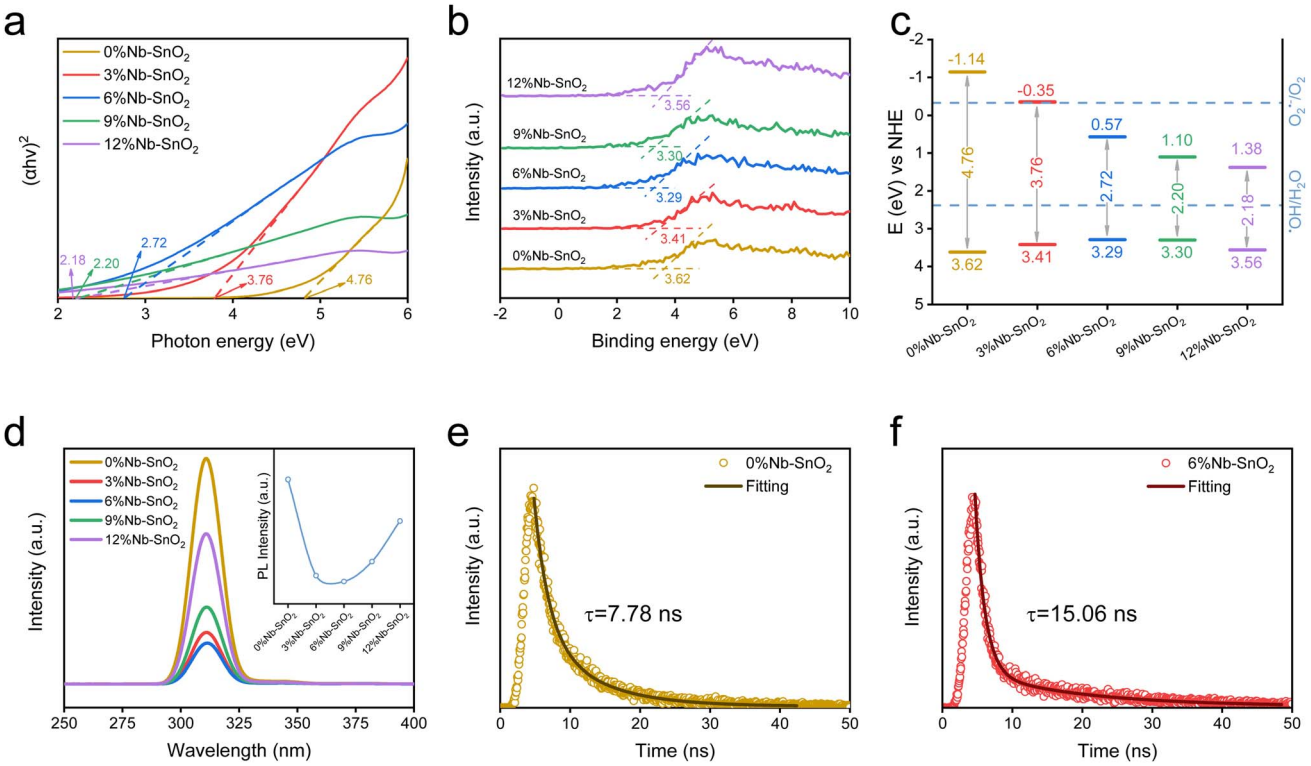

Fig. 2 Band structures and optical–electrical properties of SnO_2 QDs with Nb-induced V_O: (a) Tauc plots for bandgap evaluation; (b) XPS valence band spectra; (c) band structures; (d) photoluminescence spectra; TRPL spectra for evaluation of the carrier lifetime of (e) 0% Nb–SnO_2 and (f) 6% Nb–SnO_2.

lifetimes of 0% Nb–SnO_2 and 6% Nb–SnO_2 are further evaluated by using the TRPL spectra in Fig. 2(e) and (f). The undoped SnO_2 has a decay time of 7.78 ns, whereas 6%Nb–SnO_2 exhibits a decay time of 15.06 ns, which is almost doubled after Nb incorporation. This substantial increase in decay time suggests that Nb doping effectively prolongs the lifetime of photogenerated charge carriers. This is attributed to the defect states, which can trap charge carriers and inhibit their recombination, thereby enhancing the separation efficiency of photogenerated electron–hole pairs.[68] The extended carrier lifetime is beneficial to improve photocatalytic performance of SnO_2 QDs.

The interactive mechanism of dual defects on optical–electrical properties is discussed based on the *in situ* characterization under irradiation, as shown in Fig. 3. As depicted in Fig. 3(a), Nb incorporation exerts a significant influence on the photocurrent response of SnO_2 QDs, with the 6% Nb-doped sample demonstrating superior and stable photocurrent compared to the undoped one. This Nb-induced modification introduces both Nb^{5+} ions and V_O-related states, effectively generating multiple defect energy levels within the bandgap. Such states facilitate the capture of photogenerated electrons and holes, thereby attenuating their direct recombination pathways, as corroborated by the PL results in Fig. 2(d), and markedly enhancing the photocurrent response. Furthermore, the 6% Nb–SnO_2 sample exhibits superior consistency in its photocurrent profile under periodic irradiation, suggesting enhanced resilience and improved long-term photostability of SnO_2 QDs.

Fig. 3(b)–(f) present the *in situ* XPS spectra of 0% Nb–SnO_2 and 6% Nb–SnO_2 samples under dark, 550 nm, 420 nm, and 260 nm illumination conditions. In undoped SnO_2, the binding energies of Sn 3d and O 1s shift by approximately 0.31 eV and 0.33 eV, respectively, under 260 nm illumination, with negligible changes under 420 nm and 550 nm irradiation. In the 6% Nb–SnO_2 sample, however, the binding energies of Sn 3d and O 1s exhibit more pronounced shifts of about 0.53 eV and 0.52 eV under 260 nm illumination, respectively, and 0.31 eV and 0.30 eV under 420 nm illumination. Additionally, the Nb 3d peaks shift by 0.53 eV and 0.32 eV under 260 nm and 420 nm irradiation, respectively. These consistent shifts across Sn 3d, O 1s, and Nb 3d under illumination reflect an enriched electron density and redistributed electronic states within the Nb-doped SnO_2 lattice, guided by the presence of both Nb and V_O. Under illumination, photogenerated electrons and holes in the QDs lead to changes in the electronic states of the chemical elements. While the undoped SnO_2 sample, with a bandgap of 4.76 eV, primarily responds to high-energy UV photons, 6% Nb-doped SnO_2 displays a reduced bandgap of 2.72 eV. This narrowed bandgap enables effective photoelectron excitation at lower photon energies (*e.g.*, 420 nm and even 550 nm), underscoring the synergistic interplay between Nb doping and V_O formation that extends the operational spectral range and enhances the optoelectronic performance.

Therefore, the interplay of Nb doping and V_O formation establishes a dual-defect regime that fundamentally enhances the optical–electrical properties of SnO_2 QDs. Nb doping

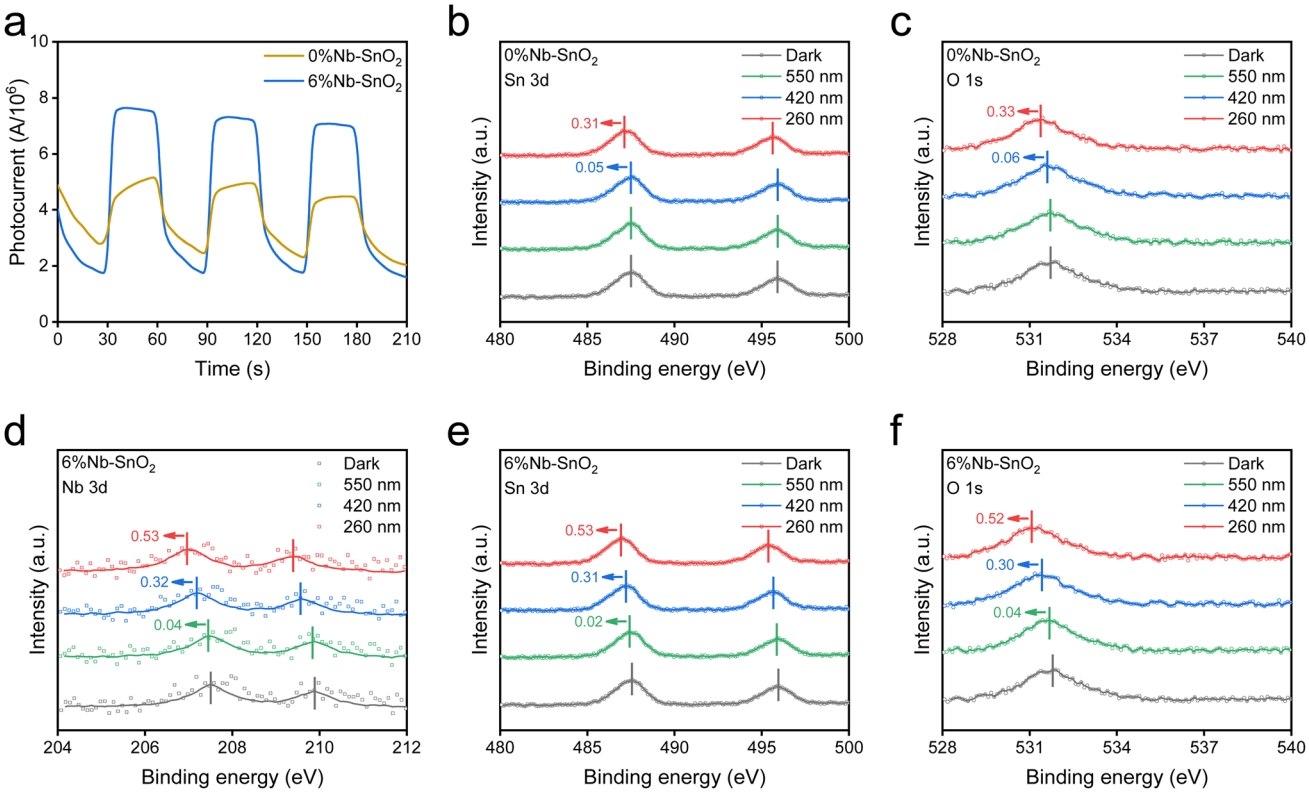

Fig. 3 *In situ* characterization of optical–electrical properties under irradiation: (a) photocurrent; XPS spectra of (b) Sn 3d and (c) O 1s of 0% Nb–SnO_2 and (d) Nb 3d, (e) Sn 3d and (f) O 1s of 6% Nb–SnO_2.

introduces additional conduction band states and defect sites, creating extended energy pathways that facilitate both the migration and spatial redistribution of photogenerated electrons. Concurrently, the Nb-induced V_O formation extends the electron lifetime by decreasing electron–hole recombination, thereby retaining more charge carriers in active states for photocatalytic reactions. The presence of Nb not only reduces the bandgap of SnO_2, enabling efficient photoexcitation under lower-energy irradiation, but also provides defect states that guide photogenerated electrons toward V_O centers, ensuring an optimized charge transfer process. This dual-defect synergy, where Nb doping and V_O formation coalesce, significantly elevates the photocatalytic performance of SnO_2 QDs, exemplifying a powerful strategy for tuning the electronic structure and extending the operational spectral range.

3.3. DFT simulated band structure and electrical properties

To further elucidate the mechanism of synergistic dual-defect band engineering, DFT-based calculations were carried out to provide insightful descriptions of the electrical properties of undoped and Nb-doped SnO_2 supercells with V_O. As depicted in Fig. 4(a) and (b), the calculated E_g of the supercells is 4.71 eV and 2.73 eV, respectively, which match well with the experimental values of 4.76 eV and 2.72 eV for the undoped and 6% Nb-doped samples. The similarity in stoichiometry and consistency in the bandgap between computational models and experimental specimens ensure the precise electronic properties revealed by DFT simulations.

TDOS and PDOS describe the contributions of Nb incorporation and oxygen defects, as shown in Fig. 4(c) and (d) as well as Fig. S7–S9.† In the undoped SnO_2 supercell, the valence band is primarily composed of Sn atoms, while both Sn and O contribute to the conduction band. With the incorporation of Nb atoms, the E_g of the supercell reduces to 2.73 eV due to contributions from O and Nb elements. Specifically, the s and p orbitals in O atoms, as well as the d orbitals in Nb atoms, extend the E_C towards the Fermi level, as shown in Fig. 4(d). Thus, the mechanism of band structure engineering could be summarized in two steps: (1) Nb incorporation establishes a defect energy level (E_D) below the conduction band; (2) the gap between E_D and E_C is filled by the V_O, which are introduced by Nb substitution. Consequently, Nb incorporation accomplishes band structure engineering by reducing the bandgap of SnO_2 QDs and enhancing the visible-light response for photocatalysis.

The charge transfer details in undoped and Nb-doped SnO_2 supercells with V_O are revealed by the Mulliken population distributions in Table 1, which are demonstrated by the visible differential charge density in Fig. 4(e)–(h). In undoped SnO_2, the charge density is relatively uniform around the Sn and O atoms, with localized electron deficiencies around oxygen vacancies. In contrast, Nb-doped SnO_2 shows significant charge redistribution, with increased electron density around V_O stimulated by Nb atoms. Thus, the synergistic effect between Nb incorporation and oxygen vacancies enhances electronic interactions in Nb-doped SnO_2. Nb atoms introduce new conduction band

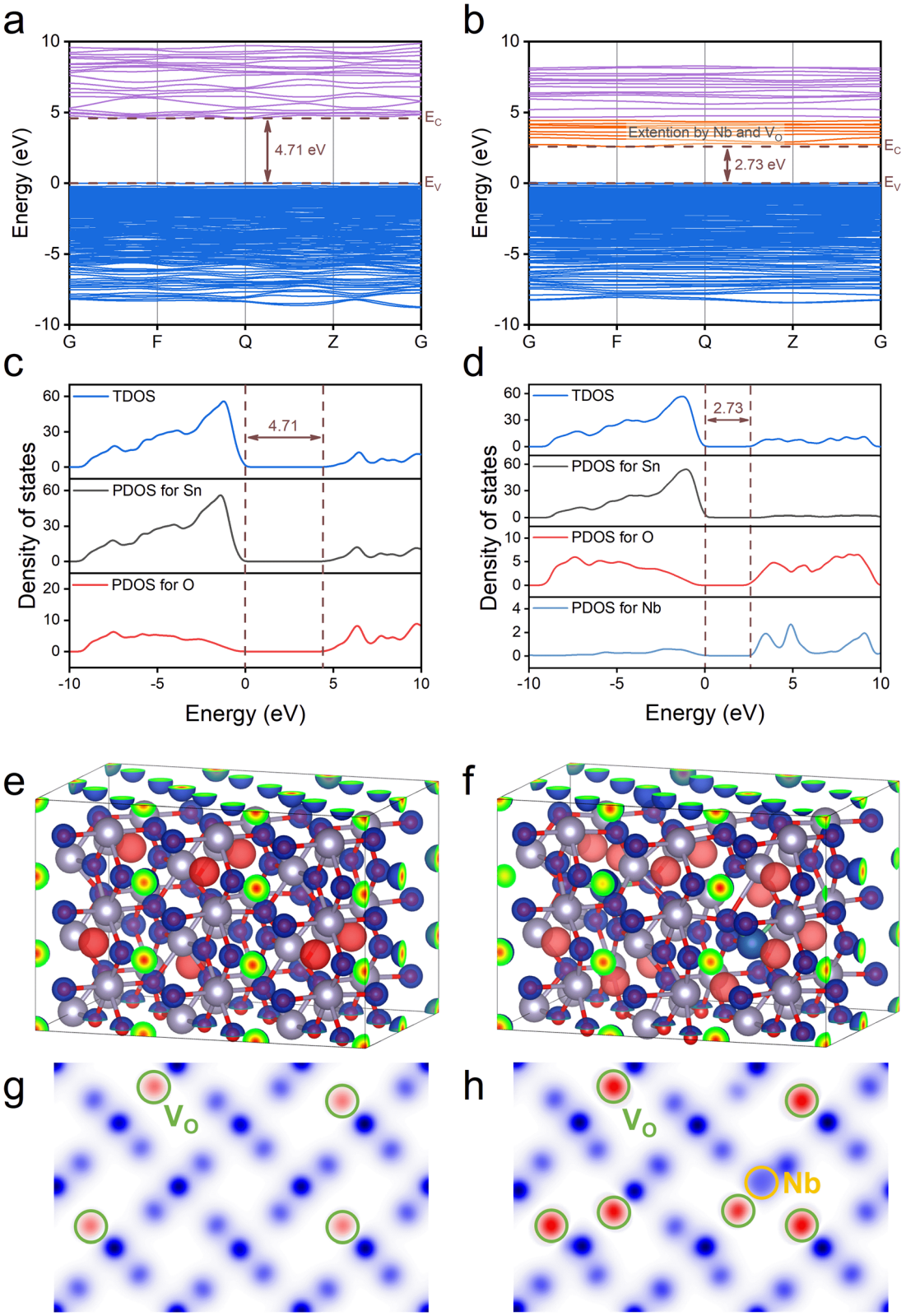

Fig. 4 DFT simulated electrical properties of undoped (left column) and Nb-doped (right column) SnO_2 super cells with VO: (a and b) band structure; (c and d) TDOS and PDOS; (e and f) differential charge density and (g and h) specific profile with V_O and Nb.

states and defect states, which have a strong ability to capture photogenerated electrons. Oxygen vacancies act as electron traps, extending the lifetime of photogenerated carriers and reducing electron–hole recombination. The synergy includes a reduced bandgap, which allows excitation under a broader light spectrum, including visible light. Consequently, the

Table 1 Mulliken population distribution and charge transfer of undoped and Nb-doped SnO_2 supercells

Supercell	Element	Coordination	Electrons	Charge transfer (e)
Undoped SnO_2	O	Full	7.22	1.22
	O	Vo	7.20	1.20
	Sn	Full	11.57	−2.43
	Sn	Vo	11.97	−2.03
Nb-doped SnO_2	O	Full	7.21	1.21
	O	Vo	7.20	1.20
	O	Nb	7.16	1.16
	O	Nb & Vo	7.17	1.17
	Sn	Full	11.57	−2.43
	Sn	Vo	12.04	−1.96
	Sn	2 Vo	12.46	−1.54
	Nb	Vo	10.75	5.75

charge separation efficiency is improved, significantly enhancing the photocatalytic performance of Nb-doped SnO_2 QDs.

3.4. Visible-light driven photocatalytic degradation of MPs

Dual-defect band structure engineering significantly improves the optical–electrical properties of SnO_2 QDs, which are prospective in photocatalytic activities. Before PE photodegradation, the photocatalytic properties of Nb-doped SnO_2 QDs under visible-light irradiation were evaluated using methylene orange (MO) dye. The experimental details and results are described in the ESI,† which indicates that the rational incorporation of Nb significantly enhances the photocatalytic abilities of SnO_2 QDs. Among the various Nb doping concentrations, 6% Nb–SnO_2 exhibits the highest photocatalytic efficiency. This optimal performance is attributed to the balanced introduction of Nb dopants and induced V_O, which effectively modulate the band structure without creating excessive recombination centers. At 6% doping, the density of defect states is sufficient to enhance visible-light absorption and facilitate efficient separation of photogenerated electron–hole pairs, as evidenced by the significantly increased rate constants k_1 and k_2 (6.25 times and 56.08 times, respectively) compared to those of undoped SnO_2, as shown in Fig. S10.† Beyond this concentration, higher Nb doping levels may lead to an increase in recombination sites created by lattice distortion, thereby diminishing the photocatalytic performance. Additionally, Fig. S11† shows that 6% Nb–SnO_2 maintains excellent long-term stability, with only a slight decrease in degradation efficiency after 90 days. These results collectively indicate that 6% Nb–SnO_2 strikes an optimal balance between defect density and charge carrier dynamics, leading to superior photocatalytic performance.

The optimized 6% Nb–SnO_2 was selected to conduct visible-light driven photocatalytic degradation of MPs and the photodegradation performance is presented in Fig. 5(a). The degradation efficiency reaches 1.1% and 28.9% after 7 hours of irradiation using a LED and Xe lamp, respectively. The corresponding rate constants are calculated to be 0.001 h^{-1} and 0.033 h^{-1}, as shown in Fig. S12(a).† Furthermore, the Nb-doped photocatalyst shows excellent repeatability in four degradation cycles as shown in Fig. S12(b).† The morphologies of MPs observed from the optical microscope and SEM images before and after photocatalytic degradation are shown in Fig. S13† for comparison. The MPs subjected to photocatalysis appear transparent, indicating a reduction in thickness. Additionally, the presence of cracks on the surface demonstrates the disruption of the assembly of PE molecules.

Other methods were used to confirm the photodegradation of MPs under visible light by Nb-doped SnO_2 QDs. The FTIR spectra in Fig. 5(b) indicate the characteristic peaks of long alkyl chains in PE.[69] The peaks at 2920 and 2851 cm^{-1} are attributed to the symmetric and asymmetric intense stretching of $-CH_2$ groups.[70] The peak at 1468 cm^{-1} indicates the stretching of the –C=C– bond while the peak at 721 cm^{-1} denotes the medium type rocking deformation of $-CH_2$.[71] An emerging peak of the hydroxyl group at 3443 cm^{-1} is due to the formation of a hydroxyl group during photocatalytic degradation.[72] The variation of characteristic peaks in FTIR spectra demonstrates the photocatalytic degradation of PE. The carbonyl index (CI) was determined by using the ratio of the area under the absorbance of 1710 cm^{-1} to the area under the reference peak at 1380 cm^{-1}.[73] The CI increases 75% from 1.325 to 2.322 for the samples before and after photocatalytic degradation. TOC analysis was carried out to further confirm the mineralization of PE before and after 7-hour irradiation by a Xe lamp, as shown in Fig. 5(c). Compared to the mass loss of 28.9%, the TOC decreases by 17.6%, from 0.92 to 0.76 mg mL^{-1}. It is inferred that parts of the PE are completely mineralized to CO_2 and H_2O while the other parts are transformed into intermediate products in the aqueous solution. The final gaseous product of PE degradation is measured by GC, as shown in Fig. 5(d). The production of CO_2 demonstrates the delay kinetics, which is ascribed to the formation and degradation of intermediates during photocatalytic degradation.

The photocatalytic PE degradation performances of 6%Nb-doped SnO_2 QDs in various water matrices are shown in Fig. 5(f). It is observed that the photocatalysts with dual defects maintain more than 80% of the original degradation capability in various water matrices such as recycled water, lake water and seawater. Although there are decreases in photocatalytic degradation efficiency, the 6%Nb-doped SnO_2 QDs are applicable in actual scenarios with complex water matrices. The excellent anti-interference ability to external species in water matrices can be ascribed to the large zeta potential in a neutral environment as well as the insignificant adsorption energy of cations on SnO_2 QDs with dual defects. As shown in Fig. S14,† the point of zero charge is at pH = 3.64 and the zeta potential is over −35 mV at pH = 7∼8, which is the common value of lake water and seawater. The electrostatic repulsion between photocatalysts and anions prevents their interaction and thus enhances anti-interference ability of the latter species. The adsorption energies of various possible metal cations are calculated by DFT computations, as exhibited in Table S2.† All adsorption energies of these cations show positive values, indicating the unlikelihood for the metal species to interact with photocatalysts in aqueous solution with salts. Therefore,

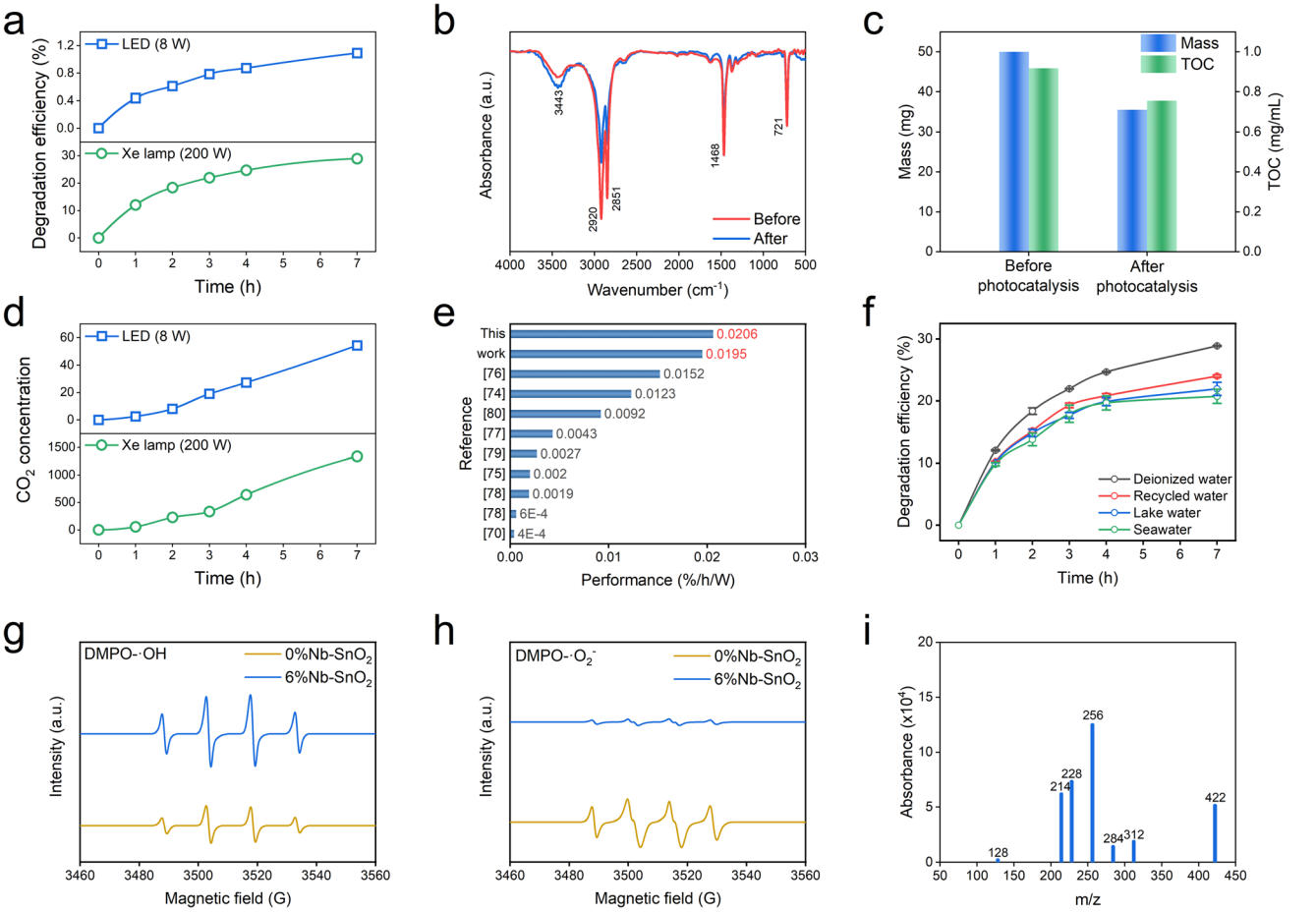

Fig. 5 Photocatalytic degradation of MPs by SnO_2 QDs with Nb-induced VO: (a) degradation efficiency under 8 W and 200 W irradiation; (b) FTIR spectra before and after 4 h irradiation; (c) mass loss and TOC analysis; (d) CO_2 product amount; (e) performance comparison with other reports; (f) degradation in various realistic aqueous environments; (g) ESR spectra of $^{\bullet}OH$; (h) ESR spectra of $^{\bullet}O_2^-$; (i) GC-MS for intermediate determination.

the present Nb-doped SnO_2 QDs are able to resist interference from influencing species and maintain excellent stability in actual water matrices.

Fig. 5(e) and Table S3† provide a comparison of the visible-light driven photocatalytic degradation performances of MPs using the current Nb–SnO_2 with those reported in previous studies.[70,74–80] In this comparison, the photocatalytic performance of photocatalysts is defined as the degradation efficiency per hour under unit power of irradiation. It is evident that the present Nb-doped oxygen-deficient SnO_2 QDs with dual defects exhibit superior photocatalytic performance in the degradation of MPs. Moreover, the 6% Nb–SnO_2 QDs before and after photocatalytic degradation of MPs for 4 hours are characterized in Fig. S15,† which demonstrates excellent stability of microstructural, compositional and optical properties for recycling of photocatalysts.

3.5. Photocatalytic mechanism of MP degradation

Synergistic dual-defect engineering by Nb-induced V_O not only reduces the bandgap but also provides abundant defect states for electron transitions and increases the lifetimes of photogenerated carriers, thereby facilitating highly efficient visible-light-driven photocatalytic degradation of MPs, even in realistic aqueous environments. The engineered band structure determines the active radicals during photocatalytic degradation. Fig. 5(g) and (h) display the ESR spectra of hydroxyl radicals ($^{\bullet}OH$) and superoxide radicals ($^{\bullet}O_2^-$) during the photocatalytic degradation of MPs. 0% Nb–SnO_2 generates both radicals upon light excitation, though the signals for both are moderate. In contrast, 6% Nb–SnO_2 exhibits a strong capability for generating $^{\bullet}OH$ radicals. The E_V of 6% Nb–SnO_2 is 3.29 eV, exceeding the 2.38 eV threshold required for $^{\bullet}OH$ generation, thereby enabling effective production of $^{\bullet}OH$ under illumination. It is noted that 6% Nb–SnO_2 displays a weak $^{\bullet}O_2^-$ signal. The pronounced enhancement in the $^{\bullet}OH$ signal and the attenuation of the $^{\bullet}O_2^-$ signal in 6%Nb–SnO_2 can be attributed to the intricate synergistic modifications to the band structure. Nb incorporation introduces additional conduction band states and defect states from induced V_O, leading to a lowering of E_C while maintaining E_V. This reduction in the bandgap allows for excitation of valence band electrons by visible light, resulting in substantial photogenerated holes, which react with water to

form ˙OH. Although the elevated E_C in the Nb-doped sample is less favorable for $^{\cdot}O_2^-$ formation, the increased generation of ˙OH compensates for this, enhancing the overall photocatalytic efficiency of MP degradation.

Fig. S16† illustrates the electrostatic potential distribution of PE, which ranges from −0.03 (blue) to +0.03 (red), representing different electrostatic potentials. The red regions indicate areas of concentrated positive charge, typically around carbon–hydrogen bonds, while the blue regions denote areas of concentrated negative charge with higher electron density. The present Nb–SnO_2 QDs with a zeta potential of −35 mV have a negatively charged surface, which facilitates the adsorption of the positively charged regions of PE, thereby enhancing the interaction between photocatalysts and targets. During the photocatalytic degradation process, hydroxyl radicals (˙OH) serve as the primary reactive species. Due to their strong oxidizing properties, they preferentially react with the positively charged regions (red areas), attacking the carbon–hydrogen bonds and subsequently leading to the cleavage of the PE chains.

The intermediate products of PE degradation are analyzed and identified using GC-MS from the solution sample after photocatalysis under 4 hours of visible-light irradiation by a Xe lamp, as revealed in Fig. 5(i). The GC-MS spectrum confirms the presence of several intermediate products, including triacontane ($m/z = 422$), octadecanoic acid ethyl ester ($m/z = 312$), octadecanoic acid ($m/z = 284$), hexadecanoic acid ethyl ester ($m/z = 284$), *n*-hexadecanoic acid ($m/z = 256$), tetradecanoic acid ($m/z = 228$), tridecanoic acid ($m/z = 214$), and octanal ($m/z = 128$), as listed in Table S4.†

Based on the above results, the photodegradation pathway and mechanism of PE in a visible-light driven photocatalytic process are illustrated in Fig. 6. Initially, the PE is decomposed by ˙OH into $C_{30}H_{62}$, which is further degraded by $O_2^{\cdot -}$ to form $C_{20}H_{40}O_2$. There are two possible routes for the degradation of $C_{20}H_{40}O_2$. One involves its reaction with ˙OH, resulting in the formation of $C_{18}H_{36}O_2$. The other route involves its interaction with another PE chain structure, yielding $C_{18}H_{32}O_2$. Simultaneously, the associated PE chain is decomposed into $C_{30}H_{62}$. Both $C_{18}H_{36}O_2$ and $C_{18}H_{32}O_2$ undergo further degradation to produce $C_{16}H_{32}O_2$, which subsequently reacts with ˙OH to form $C_{14}H_{28}O_2$ and $C_{13}H_{26}O_2$. The latter compound is then disassembled into the small molecule $C_8H_{16}O$, which ultimately undergoes mineralization into CO_2 and H_2O.

The main chemical process involved in the photocatalytic degradation of PE can be summarized as a series of steps described by using eqn (4)–(8). Initially, PE is exposed to ˙OH radicals, causing the breaking of certain chemical bonds and

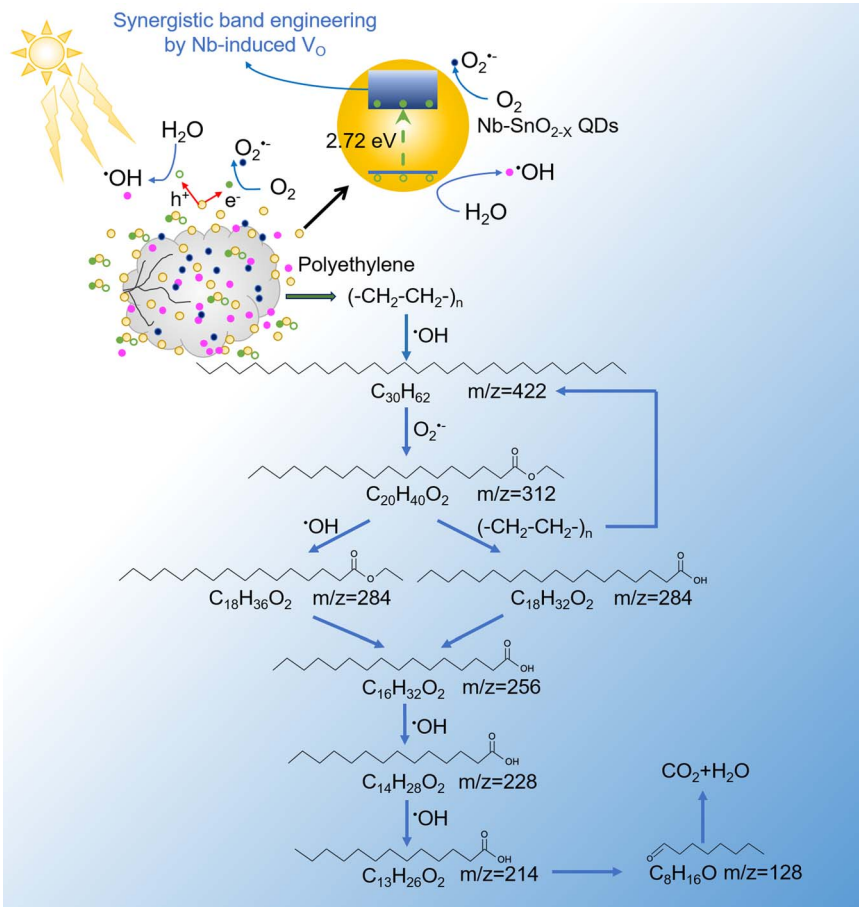

Fig. 6 Pathway and mechanism of visible-light driven photocatalytic degradation of PE by SnO_2 QDs with synergistic band engineering by Nb-induced V_O.

leaving behind polyethylene alkyl ($[-^{\bullet}CH_2CH_2-]_n$) radicals, as shown in eqn (4). These resulting radicals then react with oxygen, leading to the formation of peroxyl radicals, as depicted in eqn (5). The peroxyl radicals have the ability to capture a hydrogen (H) atom from another PE chain. The radical that undergoes this transformation produces perhydrol products, while the PE chain that loses the H atom becomes polyethylene alkyl, as illustrated in eqn (6). The weak O–O bond in the perhydrol products is prone to breaking, generating new radicals, as described by eqn (7). Moreover, these newly formed radicals exhibit higher reactivity compared to the peroxyl radicals, enabling them to capture H atoms from other PE chains, as shown in eqn (8). The key kinetics of the degradation process are determined by the rate at which intermediate radicals in eqn (6) capture H atoms. Additionally, the perhydrol products play a crucial role in the degradation process, as each perhydrol intermediate may produce two additional radicals that participate in subsequent processes.

$$[-CH_2CH_2-]_n + {}^{\bullet}OH \rightarrow [-{}^{\bullet}CH_2CH_2-]_n + H_2O \quad (4)$$

$$[-{}^{\bullet}CH_2CH_2-]_n + O_2 \rightarrow [-CH_2-HCOO^{\bullet}-CH_2-]_n \quad (5)$$

$$[-CH_2-HCOO^{\bullet}-CH_2-]_n + [-CH_2CH_2-]_n \rightarrow [-CH_2-CHCOOH-CH_2-]_n + [-{}^{\bullet}CH_2CH_2-]_n \quad (6)$$

$$[-CH_2-CHCOOH-CH_2-]_n \rightarrow [-CH_2-HCO^{\bullet}-CH_2-]_n + {}^{\bullet}OH \quad (7)$$

$$[-CH_2-HCO^{\bullet}-CH_2-]_n + [-CH_2CH_2-]_n \rightarrow [-{}^{\bullet}CH_2CH_2-]_n + [-CH_2-HCOH-CH_2-]_n \quad (8)$$

On the basis of the above results, the mechanism of visible-light driven photocatalytic degradation of PE by Nb-doped SnO_2 QDs is illustrated as Fig. 6. The introduction of Nb on SnO_2 QDs promotes the formation of V_O in the crystallites and both defects introduce energy levels, effectively extending the conduction band edge to the Fermi level. This modification results in a reduced band gap, enhancing the semiconductor's response to visible light and providing efficient photocatalytic capabilities for degrading PE. The primary active radicals, $^{\bullet}OH$, attack the carbon chains within the PE, leading to their degradation into $C_{30}H_{62}$ intermediates. Subsequently, these intermediates undergo further decomposition into smaller molecules, ultimately mineralizing into CO_2 and H_2O through a series of successive chemical processes, as depicted in Fig. 6.

4. Conclusions

This work demonstrates the synergistic dual-defect band engineering to delocalize carriers in Nb-doped SnO_2 QDs for the efficient photocatalytic degradation of MPs. The mechanism of dual-defect band engineering is comprehensively elucidated, revealing the synergistic interaction between Nb and V_O defects. Nb is found to establish donor levels within the bandgap, while V_O occupies the gap between the donor levels and the conduction band, extending the conduction band edge and resulting in a reduced bandgap responsive to visible light. Nb incorporation facilitates V_O formation, optimizing the charge carrier distribution within the confined QD matrix and doubling the lifetime of carriers. The synergistic effect between Nb and V_O significantly enhances the photoresponsive performance of SnO_2 QDs. The Nb-doped SnO_2 QDs exhibit a superior visible-light-driven MP degradation efficiency of 28.9% in 7 hours, which is maintained in various water matrices. Detailed analysis of the intermediate products formed during the degradation of PE and the elucidation of the degradation pathway has been thoroughly conducted, revealing the photocatalytic degradation mechanism of PE by Nb-doped oxygen-deficient SnO_2 QDs. Synergistic dual-defect band engineering not only facilitates efficient visible-light-driven photocatalytic degradation of MPs but also sheds light on the mechanisms of dual-defect band engineering, offering valuable insights for the design and optimization of nanoscale photocatalysts.

Data availability

The data supporting this article have been included as part of the ESI.†

Author contributions

Jianqiao Liu: conceptualization, investigation, writing – original draft. Dan Zhao: methodology, investigation. Xian Wu: methodology, investigation. Di Wu: software. Ningning Su: methodology, investigation. Yang Wang: data curation. Fang Chen: writing – review & editing. Ce Fu: supervision. Junsheng Wang: funding acquisition, writing – review & editing. Qianru Zhang: supervision, writing – review & editing.

Conflicts of interest

There are no conflicts to declare.

Acknowledgements

This work was financially supported by the Liaoning Applied Fundamental Research Project (Grant No. 2022JH2/101300158 and 2023JH2/101300014) and the Fundamental Research Funds for the Central Universities (Grant No. 3132023506 and 3132024243). The authors also appreciate Duo Zhang, Chaoting Lu and other technicians from Hongzhiwei Technology (Shanghai) Co. Ltd for their support in DFT calculations.

References

1 A. A. Horton, A. Walton, D. J. Spurgeon, E. Lahive and C. Svendsen, Microplastics in freshwater and terrestrial environments: Evaluating the current understanding to identify the knowledge gaps and future research priorities, *Sci. Total Environ.*, 2017, **586**, 127–141.

2 Y. Su, C. Yang, S. Wang, H. Li, Y. Wu, B. Xing and R. Ji, Mechanochemical formation of poly(melamine-formaldehyde) microplastic fibers during abrasion of cleaning sponges, *Environ. Sci. Technol.*, 2024, **58**, 10764–10775.

3 M. Cole, P. Lindeque, C. Halsband and T. S. Galloway, Microplastics as contaminants in the marine environment: A review, *Mar. Pollut. Bull.*, 2011, **62**, 2588–2597.
4 K. H. D. Tang, R. Li, Z. Li and D. Wang, Health risk of human exposure to microplastics: a review, *Environ. Chem. Lett.*, 2024, **22**, 1155–1183.
5 M. Eriksen, L. C. M. Lebreton, H. S. Carson, M. Thiel, C. J. Moore, J. C. Borerro, F. Galgani, P. G. Ryan, *et al.*, Plastic pollution in the world's oceans: More than 5 trillion plastic pieces weighing over 250,000 tons afloat at sea, *PLoS One*, 2014, **9**, e111913.
6 G. Kutralam-Muniasamy, V. C. Shruti, F. Pérez-Guevara and P. D. Roy, Microplastic diagnostics in humans: "The 3Ps" Progress, problems, and prospects, *Sci. Total Environ.*, 2023, **856**, 159164.
7 K. Zhang, J. Su, X. Xiong, X. Wu, C. Wu and J. Liu, Microplastic pollution of lakeshore sediments from remote lakes in Tibet plateau, China, *Environ. Pollut.*, 2016, **219**, 450–455.
8 A. Cózar, F. Echevarría, J. I. González-Gordillo, X. Irigoien, B. Úbeda, S. Hernández-León, Á. T. Palma, S. Navarro, *et al.*, Plastic debris in the open ocean, *Proc. Natl. Acad. Sci. U. S. A.*, 2014, **111**, 10239–10244.
9 H. T. Pinheiro, C. MacDonald, R. G. Santos, R. Ali, A. Bobat, B. J. Cresswell, R. Francini-Filho, R. Freitas, *et al.*, Plastic pollution on the world's coral reefs, *Nature*, 2023, **619**, 311–316.
10 A. L. Lusher, V. Tirelli, I. O'Connor and R. Officer, Microplastics in Arctic polar waters: the first reported values of particles in surface and sub-surface samples, *Sci. Rep.*, 2015, **5**, 14947.
11 N. Simon, K. Raubenheimer, N. Urho, S. Unger, D. Azoulay, T. Farrelly, J. Sousa, H. van Asselt, *et al.*, A binding global agreement to address the life cycle of plastics, *Science*, 2021, **373**, 43–47.
12 R.-Z. Wang, Z. Lin, Y.-Q. Wang, K.-N. Zhang, G.-H. Zhang, J. Zhang, S. S. Mao and S.-H. Shen, A direct polymeric carbon nitride/tungsten oxide Z-scheme heterostructure for efficient photocatalytic hydrogen generation via reforming of plastics into value-added chemicals, *Rare Met.*, 2024, **43**, 3771–3783.
13 Q. Xu, Q.-S. Huang, T.-Y. Luo, R.-L. Wu, W. Wei and B.-J. Ni, Coagulation removal and photocatalytic degradation of microplastics in urban waters, *Chem. Eng. J.*, 2021, **416**, 129123.
14 J. Liu, X. Qu, C. Zhang, W. Dong, C. Fu, J. Wang and Q. Zhang, High-yield aqueous synthesis of partial-oxidized black phosphorus as layered nanodot photocatalysts for efficient visible-light driven degradation of emerging organic contaminants, *J. Cleaner Prod.*, 2022, **377**, 134228.
15 R. Xu, L. Cui and S. Kang, Countering microplastics pollution with photocatalysis: Challenge and prospects, *Prog. Nat. Sci.:Mater. Int.*, 2023, **33**(3), 251–266.
16 A. Uheida, H. G. Mejía, M. Abdel-Rehim, W. Hamd and J. Dutta, Visible light photocatalytic degradation of polypropylene microplastics in a continuous water flow system, *J. Hazard. Mater.*, 2021, **406**, 124299.
17 W. H. Lee, C. W. Lee, G. D. Cha, B.-H. Lee, J. H. Jeong, H. Park, J. Heo, M. S. Bootharaju, *et al.*, Floatable photocatalytic hydrogel nanocomposites for large-scale solar hydrogen production, *Nat. Nanotechnol.*, 2023, **18**, 754–762.
18 J. Wang, M. Sun, C. Liu, Y. Ye, M. Chen, Z. Zhao, Y. Zhang, X. Wu, *et al.*, Customized microenvironments spontaneously facilitate coupled engineering of real-life large-scale clean water capture and pollution remediation, *Adv. Mater.*, 2023, **35**, 2306103.
19 X. Zhang, F. Wu, G. Li, L. Wang, J. Huang, A. Meng and Z. Li, Modulating electronic structure and sulfur p-band center by anchoring amorphous Ni@NiSx on crystalline CdS for expediting photocatalytic H_2 evolution, *Appl. Catal., B*, 2024, **342**, 123398.
20 L. Zhang, Z. Jiang, J. Guo, C. Zhang, X. Xu, D. Shi, Y. Shao, Z. Ai, *et al.*, Deep insight into regulation mechanism of band distribution in phase junction CdS for enhanced photocatalytic H_2 production, *J. Colloid Interface Sci.*, 2024, **669**, 146–156.
21 H. Fu, Y. Xiao, A. Abulizi, K. Okitsu and T. Ren, Diethanolamine-functionalized BiOI hollow microspheres with negative conduction bands maximize the visible light photocatalytic performance for CO_2 reduction, *J. Alloys Compd.*, 2024, **984**, 173882.
22 J. Liu, J. Lv, J. Shi, L. Wu, N. Su, C. Fu and Q. Zhang, Size effects of tin oxide quantum dot gas sensors: From partial depletion to volume depletion, *J. Mater. Res. Technol.*, 2020, **9**, 16399–16409.
23 J. Liu, Z. Zhai, G. Jin, Y. Li, F. F. Monica and X. Liu, Simulation of the grain size effect in gas-sensitive SnO_2 thin films using the oxygen vacancy gradient distribution model, *Electron. Mater. Lett.*, 2015, **11**, 34–40.
24 J. Liu, Y. Gao, X. Wu, G. Jin, Z. Zhai and H. Liu, Inhomogeneous oxygen vacancy distribution in semiconductor gas sensors: Formation, migration and determination on gas sensing characteristics, *Sensors*, 2017, **17**, 1852.
25 Y. Guo, H. Wen, T. Zhong, H. Huang and Z. Lin, Edge-rich atomic-layered BiOBr quantum dots for photocatalytic molecular oxygen activation, *Chem. Eng. J.*, 2022, **445**, 136776.
26 P. Sun, Z. Xing, Z. Li and W. Zhou, Recent advances in quantum dots photocatalysts, *Chem. Eng. J.*, 2023, **458**, 141399.
27 W. Han, H. Zhang, D. Li, W. Qin, X. Zhang, S. Wang and X. Duan, Surface engineered carbon quantum dots for efficient photocatalytic hydrogen peroxide production, *Appl. Catal., B*, 2024, **350**, 123918.
28 L. Zhao, P. Zhang, L. Li, N. Li, R. Tuerhong, X. Su, W. Sun and L. Han, Revealing the potential of quantum dot nanomaterials in photocatalytic applications, *Chemosphere*, 2024, **361**, 142547.
29 S. Guo, Y. Ji, Y. Li, H. Li, P. An, J. Zhang, J. Yan, S. Liu, *et al.*, Amorphous quantum dots co-catalyst: Defect level induced solar-to-hydrogen production, *Appl. Catal., B*, 2023, **330**, 122583.

30 Y. Wang, X. Wu, J. Liu, Z. Zhai, Z. Yang, J. Xia, S. Deng, X. Qu, *et al.*, Mo-modified band structure and enhanced photocatalytic properties of tin oxide quantum dots for visible-light driven degradation of antibiotic contaminants, *J. Environ. Chem. Eng.*, 2022, **10**, 107091.

31 J. Shao, K. Deng, L. Chen, C. Guo, C. Zhao, J. Cui, T. Shen, K. Li, *et al.*, Aqueous synthesis of Nb-modified SnO_2 quantum dots for efficient photocatalytic degradation of polyethylene for in situ agricultural waste treatment, *Green Process. Synth.*, 2021, **10**, 499–506.

32 S.-K. Le, Q.-J. Jin, J.-A. Han, H.-C. Zhou, Q.-S. Liu, F. Yang, J. Miao, P.-P. Liu, *et al.*, Rare earth element-modified MOF materials: synthesis and photocatalytic applications in environmental remediation, *Rare Met.*, 2024, **43**, 1390–1406.

33 Y. Gao, Y. Li, L. Shangguan, Z. Mou, H. Zhang, D. Ge, J. Sun, F. Xia, *et al.*, Optimizing the band structure of sponge-like S-doped poly(heptazine imide) with quantum confinement effect towards boosting visible-light photocatalytic H_2 generation, *J. Colloid Interface Sci.*, 2023, **644**, 116–123.

34 S. Fatima, M. Anwar, A. S. A. Almalki, A. Alhadhrami, M. F. Warsi and Z. M. El-Bahy, Fabrication of rare earth (Tb^{+3}) and alkaline earth metal (Mg^{+2}) Co-doped $CdAl_2O_4$@MXene composite: A unique approach to tune bandgap energy through quantum confinement effect for photocatalytic applications, *Ceram. Int.*, 2024, **50**, 29201–29212.

35 H.-Y. Zhao, S. Wang, H.-Y. Zhu, X.-X. Zhang, D.-H. Shang, X.-W. Zhou, J. Wang, C.-Z. Zhu, *et al.*, Modulating nanograin size and oxygen vacancy of porous ZnO nanosheets by highly concentrated Fe-doping effect for durable visible photocatalytic disinfection, *Rare Met.*, 2024, **43**, 5905–5920.

36 C.-Z. Zhu, Q.-H. Tian, B.-H. Wang, M.-T. Xu, Q.-J. Jin, Z.-Y. Zhang, S.-K. Le, Y. Wu, *et al.*, Application of modified cerium dioxide for photocatalytic air pollution purification, *Rare Met.*, 2024, **43**, 5473–5486.

37 Y. Zhang, J. Di, X. Qian, M. Ji, Z. Tian, L. Ye, J. Zhao, S. Yin, *et al.*, Oxygen vacancies in $Bi_2Sn_2O_7$ quantum dots to trigger efficient photocatalytic nitrogen reduction, *Appl. Catal., B*, 2021, **299**, 120680.

38 Y. Song, Z. Li, S. Li, C. Yang, L. Huang, X. Zhang, Q. Wang and H. Zhang, Enhancing the photocatalytic efficiency of sulfamethoxazole by regulating the band gap structure of g-C_3N_4 through phosphorus element doping, *J. Water Proc.Engineering*, 2024, **58**, 104936.

39 S. Yang, X. Guo, K. Liu, Y. Li, T. Li, X. Gu, R. Arenal, X. Zheng, *et al.*, Size effect of CoS_2 cocatalyst on photocatalytic hydrogen evolution performance of g-C_3N_4, *J. Colloid Interface Sci.*, 2023, **635**, 305–315.

40 J. Liu, Y. Bai, J. Shi, Q. Yu, J. Liu, J. Yang, C. Fu and Q. Zhang, Selective detection of mercury ions based on tin oxide quantum dots: Performance and fluorescence enhancement model, *J. Mater. Chem. C*, 2021, **9**, 8274–8284.

41 J. Zhao, S. Wu, J. Liu, H. Liu, S. Gong and D. Zhou, Tin oxide thin films prepared by aerosol-assisted chemical vapor deposition and the characteristics on gas detection, *Sens. Actuators, B*, 2010, **145**, 788–793.

42 J. Liu, Q. Zhang, X. Tian, Y. Hong, Y. Nie, N. Su, G. Jin, Z. Zhai, *et al.*, Highly efficient photocatalytic degradation of oil pollutants by oxygen deficient SnO_2 quantum dots for water remediation, *Chem. Eng. J.*, 2021, **404**, 127146.

43 A. V. Nimmy, A. Mahesh, V. M. Anandakumar and V. Biju, Revealing the role of defect-induced trap levels in sol–gel-derived TiO_2 samples and the synergistic effect of a mixed phase in photocatalytic degradation of organic pollutants, *J. Phys. Chem. Solids*, 2024, **185**, 111774.

44 C. Liu, S. Mao, M. Shi, X. Hong, D. Wang, F. Wang, M. Xia and Q. Chen, Enhanced photocatalytic degradation performance of $BiVO_4$/BiOBr through combining Fermi level alteration and oxygen defect engineering, *Chem. Eng. J.*, 2022, **449**, 137757.

45 M. Trochowski, M. Kobielusz, K. Mróz, M. Surówka, J. Hämäläinen, T. Iivonen, M. Leskelä and W. Macyk, How insignificant modifications of photocatalysts can significantly change their photocatalytic activity, *J. Mater. Chem. A*, 2019, **7**, 25142–25154.

46 M. Rezaei, A. Nezamzadeh-Ejhieh and A. R. Massah, A comprehensive review on the boosted effects of anion vacancy in the heterogeneous photocatalytic degradation, Part II: Focus on oxygen vacancy, *ACS Omega*, 2024, **9**, 6093–6127.

47 C. Zhang, S. Qin, H. Gao and P. Jin, High hydrogen evolution activities of dual-metal atoms incorporated N-doped graphenes achieved by coordination regulation, *J. Mater. Inf.*, 2024, **4**, 1.

48 H. Li, C. Deng, F. Li, M. Ma and Q. Tang, Investigation of dual atom doped single-layer MoS_2 for electrochemical reduction of carbon dioxide by first-principle calculations and machine-learning, *J. Mater. Inf.*, 2023, **3**, 25.

49 Z. Zhang, W. Wang, E. Gao, M. Shang and J. Xu, Enhanced photocatalytic activity of Bi_2WO_6 with oxygen vacancies by zirconium doping, *J. Hazard. Mater.*, 2011, **196**, 255–262.

50 Q. Gao, Y. Dai, C. Li, K. Wang and X. Li, The role of oxygen vacancies in enhancement of photocatalysis and ferromagnetism of (Mn, Co) co-doped ZnO nanoparticles, *Mater. Sci. Semicond. Process.*, 2024, **181**, 108637.

51 S.-H. Cao, J.-R. Qu, Y.-Q. Zhao, Y.-T. Sun, W.-T. Gao, B. Han and Y. Lu, Visible-light-driven photocatalysis degradation of antibiotic pollutants by La-doped CeO_2 nanorods: synergy of La doping and oxygen vacancy, *Rare Met.*, 2024, **43**, 3134–3145.

52 J. Liu, W. Li, H. Li, Y. Zhang, Z. Zhai, Y. Wang, C. Fu and J. Wang, A novel detection method for sulfur content in ship fuel based on metal-doped tin oxide quantum dots as fluorescent sensor, *Fuel*, 2024, **357**, 129739.

53 X. Liu, J. Zheng, K. Peng, G. Qin, Y. Yang and Z. Huang, The intrinsic effects of oxygen vacancy and doped non-noble metal in TiO_2(B) on photocatalytic oxidation VOCs by visible light driving, *J. Environ. Chem. Eng.*, 2022, **10**, 107390.

54 P. Zhang, L. Chen, D.-H. Kuo, B. Wu, Z. Su, D. Lu, Q. Wu, J. Li, *et al.*, Photocatalytic fixation of nitrogen to ammonia with a Ce/S co-doped TiO_2 catalyst: synergistic tuning of heterovalent metal states and oxygen vacancy defects, *J. Mater. Chem. A*, 2024, **12**, 7163–7177.

55 M. Lin, H. Liu, H. Wang, J. Wu, H. Jiang, H. Wei, M. Ou, Z. Guan, *et al.*, Co dopant anchored in the $BiOIO_3$ nanosheets to induce oxygen vacancies for enhanced photocatalytic activity, *Chem. Eng. J.*, 2024, **484**, 149472.
56 Y. Wang, N. Su, J. Liu, Y. Lin, J. Wang, X. Guo, Y. Zhang, Z. Qin, *et al.*, Enhanced visible-light photocatalytic properties of SnO_2 quantum dots by niobium modification, *Results Phys.*, 2022, **37**, 105515.
57 J. Liu, Y. Nie, W. Xue, L. Wu, H. Jin, G. Jin, Z. Zhai and C. Fu, Size effects on structural and optical properties of tin oxide quantum dots with enhanced quantum confinement, *J. Mater. Res. Technol.*, 2020, **9**, 8020–8028.
58 J. Liu, W. Xue, G. Jin, Z. Zhai, J. Lv, W. Hong and Y. Chen, Preparation of tin oxide quantum dots in aqueous solution and applications in semiconductor gas sensors, *Nanomaterials*, 2019, **9**, 240.
59 B. Han and F. Li, Regulating the electrocatalytic performance for nitrogen reduction reaction by tuning the N contents in $Fe_3@N_XC_{20-X}(x=0\sim4)$: a DFT exploration, *J. Mater. Inf.*, 2023, **3**, 24.
60 L. Zhang, J. Zhou and X. Chen, Data-driven exploration and first-principles analysis of perovskite material, *J. Mater. Inf.*, 2024, **4**, 13.
61 J. Liu, L. Wu, F. Gao, W. Hong, G. Jin and Z. Zhai, Size effects of vacancy formation and oxygen adsorption on gas-sensitive tin oxide semiconductor: A first principle study, *Curr. Nanosci.*, 2021, **17**, 327–337.
62 B. Wu, X. Zhang, Z. Wang, Z. Chen, S. Liu, J. Liu, Z. Xu, Q. Sun, *et al.*, Data-driven strategy for bandgap database construction of perovskites and the potential segregation study, *J. Mater. Inf.*, 2024, **4**, 7.
63 J. Liu, C. Zhang, Y. Wang, X. Chen, R. Jing, T. Song, Z. Zhang, H. Wang, *et al.*, Black phosphorus nanodot incorporated tin oxide hollow-spherical heterojunction for enhanced properties of room-temperature gas sensors, *Ceram. Int.*, 2023, **49**, 8248–8258.
64 A. R. West, *Solid State Chemistry and its Applications*, 2014.
65 A. L. Patterson, The Scherrer formula for X-ray particle size determination, *Phys. Rev.*, 1939, **56**, 978–982.
66 H. Yan, T. Liu, Y. Lv, X. Xu, J. Xu, X. Fang and X. Wang, Doping SnO_2 with metal ions of varying valence states: discerning the importance of active surface oxygen species vs. acid sites for C_3H_8 and CO oxidation, *Phys. Chem. Chem. Phys.*, 2024, **26**, 3950–3962.
67 V. Gokulakrishnan, S. Parthiban, K. Jeganathan and K. Ramamurthi, Investigations on the structural, optical and electrical properties of Nb-doped SnO_2 thin films, *J. Mater. Sci.*, 2011, **46**, 5553–5558.
68 X.-y. Yang, S.-m. Wen, D.-d. Chen, T. Li and C.-w. Zhao, First-principles study of the influence of Nb doping on the electronic structure and optoelectronic properties of β-Ga_2O_3, *Phys. Lett. A*, 2022, **433**, 128025.
69 G. Liu, D. Zhu, W. Zhou, S. Liao, J. Cui, K. Wu and D. Hamilton, Solid-phase photocatalytic degradation of polystyrene plastic with goethite modified by boron under UV–vis light irradiation, *Appl. Surf. Sci.*, 2010, **256**, 2546–2551.
70 S. S. Ali, I. A. Qazi, M. Arshad, Z. Khan, T. C. Voice and C. T. Mehmood, Photocatalytic degradation of low density polyethylene (LDPE) films using titania nanotubes, *Environ. Nanotechnol., Monit. Manage.*, 2016, **5**, 44–53.
71 T. S. Tofa, F. Ye, K. L. Kunjali and J. Dutta, Enhanced visible light photodegradation of microplastic fragments with plasmonic platinum/zinc oxide nanorod photocatalysts, *Catalysts*, 2019, **9**, 819.
72 I. Nabi, A.-U.-R. Bacha, K. Li, H. Cheng, T. Wang, Y. Liu, S. Ajmal, Y. Yang, *et al.*, Complete photocatalytic mineralization of microplastic on TiO_2 nanoparticle film, *iScience*, 2020, **23**(7), 101326.
73 M. C. Ariza-Tarazona, J. F. Villarreal-Chiu, J. M. Hernández-López, J. Rivera De la Rosa, V. Barbieri, C. Siligardi and E. I. Cedillo-González, Microplastic pollution reduction by a carbon and nitrogen-doped TiO_2: Effect of pH and temperature in the photocatalytic degradation process, *J. Hazard. Mater.*, 2020, **395**, 122632.
74 M. C. Ariza-Tarazona, J. F. Villarreal-Chiu, V. Barbieri, C. Siligardi and E. I. Cedillo-González, New strategy for microplastic degradation: Green photocatalysis using a protein-based porous N-TiO_2 semiconductor, *Ceram. Int.*, 2019, **45**, 9618–9624.
75 S.-M. Lam, J.-C. Sin, H. Zeng, H. Lin, H. Li, Y.-Y. Chai, M.-K. Choong and A. R. Mohamed, Green synthesis of Fe-ZnO nanoparticles with improved sunlight photocatalytic performance for polyethylene film deterioration and bacterial inactivation, *Mater. Sci. Semicond. Process.*, 2021, **123**, 105574.
76 A. D. Vital-Grappin, M. C. Ariza-Tarazona, V. M. Luna-Hernández, J. F. Villarreal-Chiu, J. M. Hernández-López, C. Siligardi and E. I. Cedillo-González, The role of the reactive species involved in the photocatalytic degradation of HDPE microplastics using C,N-TiO_2 powders, *Polymers*, 2021, **13**, 999.
77 R. Jiang, G. Lu, Z. Yan, J. Liu, D. Wu and Y. Wang, Microplastic degradation by hydroxy-rich bismuth oxychloride, *J. Hazard. Mater.*, 2021, **405**, 124247.
78 B. E. Llorente-García, J. M. Hernández-López, A. A. Zaldívar-Cadena, C. Siligardi and E. I. Cedillo-González, First insights into photocatalytic degradation of HDPE and LDPE microplastics by a mesoporous N–TiO_2 coating: Effect of size and shape of microplastics, *Coatings*, 2020, **10**, 658.
79 M. C. Ariza-Tarazona, C. Siligardi, H. A. Carreón-López, J. E. Valdéz-Cerda, P. Pozzi, G. Kaushik, J. F. Villarreal-Chiu and E. I. Cedillo-González, Low environmental impact remediation of microplastics: Visible-light photocatalytic degradation of PET microplastics using bio-inspired C,N-TiO_2/SiO_2 photocatalysts, *Mar. Pollut. Bull.*, 2023, **193**, 115206.
80 J. D. Acuña-Bedoya, E. Luévano-Hipólito, E. I. Cedillo-González, L. P. Domínguez-Jaimes, A. M. Hurtado and J. M. Hernández-López, Boosting visible-light photocatalytic degradation of polystyrene nanoplastics with immobilized Cu_XO obtained by anodization, *J. Environ. Chem. Eng.*, 2021, **9**, 106208.